

# Extraction of Collapsed Buildings in the 2016 Kumamoto Earthquake Using Multi-Temporal PALSAR-2 Data

Wen Liu<sup>†</sup> and Fumio Yamazaki

Department of Urban Environment Systems, Graduate School of Engineering, Chiba University  
1-33 Yayoi-cho, Inage-ku, Chiba 263-8522, Japan

<sup>†</sup>Corresponding author, E-mail: wen.liu@chiba-u.jp

[Received October 31, 2016; accepted January 19, 2017]

An earthquake (Mw6.2) struck Kumamoto Prefecture, Japan on April 14, 2016. A larger event (Mw7.0) struck the same area 28 hours later, on April 16. The series of earthquakes caused significant damage to buildings and infrastructures. Remote sensing is an effective tool to grasp damage situation over wide areas after a disaster strikes. In this study, two sets of ALOS-2 PALSAR-2 images taken before and after the earthquake were used to extract the areas with collapsed buildings. Three representative change indices, the co-event coherence, the ratio between the co- and pre-event coherence, and the z-factor combining the difference and correlation coefficients, were adopted to extract the collapsed buildings in the central district of Mashiki Town, the most severely affected area. The results of a building-by-building damage survey in the target area were used to investigate the most suitable threshold value for each index. The extracted results were evaluated by comparing them with the reference data from field surveys. Finally, the most valid factor was applied to larger affected areas for Kumamoto City and its surroundings.

**Keywords:** ALOS-2 PALSAR-2, synthetic aperture radar, coherence, intensity, damage extraction

## 1. Introduction

The 2016 Kumamoto earthquake was a series of earthquake events, including the moment-magnitude (Mw) 7.0 mainshock and the Mw6.2 foreshock [1]. The mainshock occurred in the Futagawa Fault, close to the Hinagu Fault. Thus, the first event was designated as the “foreshock” and the second one as the “mainshock.” The foreshock occurred at 21:26 (local time) on April 14, 2016. Its epicenter was shallow in depth and located at the end of the Hinagu Fault, at 32.79°N, 130.70°E [1]. Strong shaking, 7 on the Japan Meteorological Agency (JMA) seismic intensity scale, was observed in Mashiki Town (population: 33,000) and to the east of the city of Kumamoto (population: 735,000). A considerable amount of structural damage and a number of human casualties were reported, including 9 deaths [2]. Twenty-eight (28) hours later, the mainshock struck Kumamoto Prefecture at 1:25 AM on

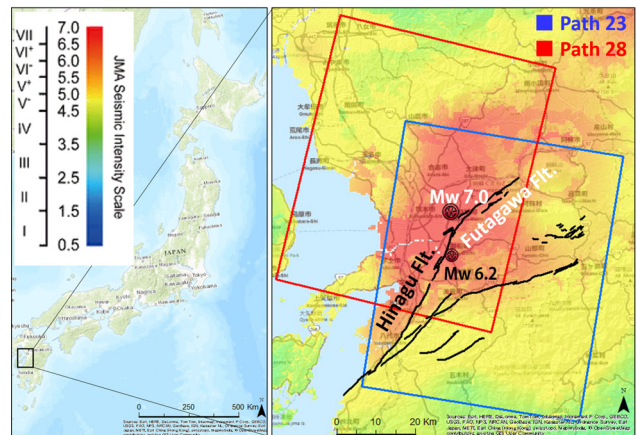


**Fig. 1.** The estimated distribution of the Instrumental JMA seismic intensity by QuiQuake [3] and the location of PALSAR-2 images used in this study.

April 16, 2016. The epicenter was located 4.5 km northwest of the foreshock. Strong motion jolted the whole of the island of Kyushu, as shown in Fig. 1 [3], with motion of JMA seismic intensity 7, the largest value on this scale, being observed at Mashiki and Nishihara [4].

Due to the strong shaking, impacts associated with the Kumamoto earthquake sequence were extensive. More than 150 landslides were reported in Kumamoto Prefecture. The largest landslide was observed in the Kawayo district of Minami-Aso village. This landslide caused the Aso-Ohashi Bridge, with a 206 m span and an 8 m width, to fall into the Kurokawa River. The earthquake also caused the suspension of road and railway networks. Kumamoto Airport was closed until April 18. Thus, it was difficult to carry out field surveys soon after the earthquake. A total of forty-nine people died and one went missing in the earthquake sequence, mostly due to the collapse of wooden houses in Mashiki and landslides in Minami-Aso. More than 8,000 buildings collapsed, and about 30,000 buildings were severely damaged. Kumamoto Castle, which is designated as an Important Cultural Property of Japan, sustained severe damage to its stone walls and roof tiles.

In recent decades, remote sensing has been used to estimate damages due to disasters. Among other sensors, synthetic aperture radar (SAR), which can operate both

day and night under all weather conditions, is an effective aid to emergency response. Various damage detection methods using multi-temporal SAR images taken before and after a disaster have been proposed [5–7]. The satellite ALOS, which carries two optical sensors and one L-band SAR sensor, was launched by the Japan Aerospace Exploration Agency (JAXA) in 2006 [8]. One of the main objectives of ALOS was worldwide disaster monitoring. Matsuoka and Estrada [9] used the single-polarization ALOS PALSAR data to evaluate damage of buildings in the 2007 Pisco, Peru earthquake. Park et al. [10] and Watanabe et al. [11] mapped urban areas affected by the 2011 Tohoku-Oki, Japan earthquake from PALSAR data in the full-polarimetric mode. The satellite ALOS-2, a follow-up mission of the ALOS program, was launched on May 24, 2014 with an enhanced high-resolution SAR sensor, PALSAR-2, aboard. Owing to the right-and-left looking function of the PALSAR-2 SAR sensor, the observation repetition frequency was improved, and it is now possible to monitor affected areas soon after disaster strikes [8]. Bahri et al. [12] used the pre-and post-event ALOS-2 PALSAR-2 imagery to assess the damage in the 2015 Gorkha, Nepal earthquake. Watanabe et al. [13] extracted damaged urban areas based on the changes in the interferometric SAR coherence of PALSAR-2 data for the same event.

In this study, six single-polarized ALOS-2 PALSAR-2 images taken before and after the 2016 Kumamoto earthquake were used to extract the areas having severe building damage. Three common change indices were adopted to evaluate the damage in Mashiki. The threshold values for building damage classification were investigated by introducing reference data from field surveys. Damage maps obtained using the different change indices were produced, and they were compared with the truth data. Then, the most suitable index and its threshold values were applied to the affected densely inhabited districts (DIDs) in Kumamoto Prefecture.

## 2. Study Area and Image Data

### 2.1. The Affected Densely Inhabited Districts (DID) in Kumamoto Prefecture

This study focused on the affected densely inhabited districts (DIDs) in Kumamoto Prefecture, the area outlined in orange in **Fig. 2**. This area includes, from north to south, Koshi, Nishigoshi, Kikuyo, Kumamoto, and Mashiki. Mashiki, located above the Futagawa Fault and one of the most affected areas, was selected as the target area. In both the foreshock and mainshock, level 7 Seismic Intensity on the JMA scale was observed in this area. A close-up of the aerial photograph taken by the Geospatial Information Authority of Japan (GSI) at 12:21 AM local time on April 16, 2018 is shown in **Fig. 3(a)**. Many blue sheets, which indicated damage, were confirmed on the top of the buildings.

A land-cover map published by JAXA is shown in

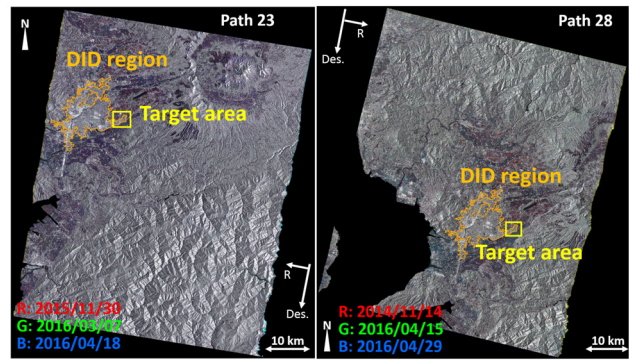


**Fig. 2.** Color composites of the geo-coded pre- and post-event PALSAR-2 backscattering coefficient images taken in paths 23 (a) and 28 (b). The orange polygons show the affected densely inhabited districts (DIDs); the yellow frame shows the target area in Mashiki.

**Fig. 3(b)** [8, 14]. About 45% of the target area was classified as the urban with buildings existing. According to the Fundamental Geospatial Data published by the GSI, there are about 5,000 buildings in this area [15]. The damage grades of 2,340 buildings were evaluated by the field surveys of the Architectural Institute of Japan (AIJ) [16]. The average ratio of collapsed buildings in each  $57\text{ m} \times 57\text{ m}$  grid-cell was calculated, as shown in **Fig. 3(c)**.

There were collapsed buildings in 155 of 414 cells. The area between the Mashiki Town Hall and the Akitsu River was severely damaged, with a building-collapse ratio of more than 50%. This damage ratio map was used as the reference data in this study.

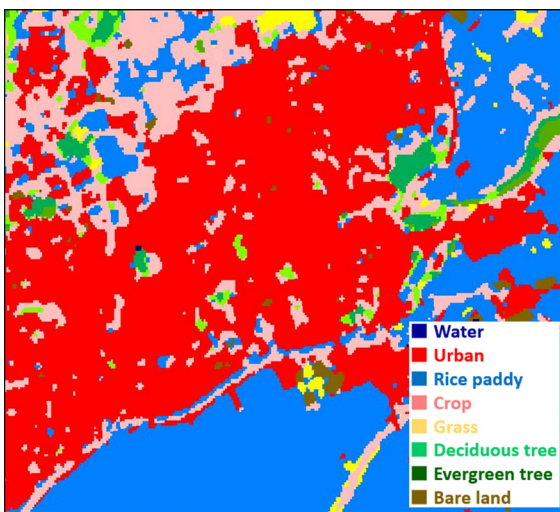
### 2.2. PALSAR-2 Data and Pre-Processing

Six pre- and post-event PALSAR-2 data were used in this study. These images were taken in StripMap mode by the HH polarization from the two different descending paths. The acquisition conditions are listed in **Table 1**. From path 23, two data were taken before the foreshock, and one was taken after the mainshock. From path 28, one data was taken before the foreshock, one was between the foreshock and mainshock, and another one was after the mainshock. They were provided as the level 1.1 data in the slant range, which were represented by complex  $I$  and  $Q$  channels to preserve the amplitude and phase information.

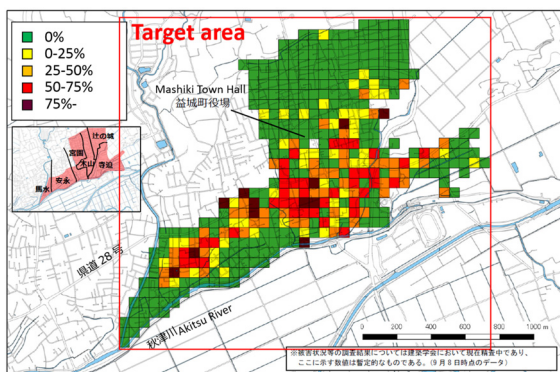
Several pre-processing steps were applied before the damage extraction. The three data in each pair were registered on a sub-pixel level. A globally available digital elevation model (SRTM: shuttle radar topography mission) was used to compensate for the image distortion caused by the terrain heights. Then they were projected onto a World Geodetic System (WGS) 84 reference ellipsoid with a resampled square pixel size of 2.5 m. The amplitude information was converted to the backscattering coefficient ( $\sigma_{na}$ ) in the dB unit, according to the calibration factor [8]. The color composites of the backscattering coefficient images are shown in



(a) Aerial photograph



(b) Land-cover map



(c) Building-collapse map

**Fig. 3.** (a) Aerial photograph of central Mashiki taken at 12:21 AM on April 16, 2016, soon after the mainshock, by the Geospatial Information Authority of Japan (GSI) [15]; (b) land-use and land-cover map of the same area published by JAXA [8,14]; (c) building-collapse map, created according to the field surveys of the Architectural Institute of Japan (AIJ) [16], was introduced as the reference data, where the damage was classified into five levels according to the percentage of collapsed buildings.

**Table 1.** Acquisition conditions of the six ALOS-2 PALSAR-2 data used in this study.

Date	Incident angle [°]	Resolution (R×A) [m]	Path	Look direction
2015/11/30				
<b>2016/03/07</b>	36.2	1.43×2.03	23	right
2016/04/18				
<b>2014/11/14</b>				
2016/04/15	32.4	1.43×1.74	28	left
2016/04/29				

\*Bold font represents the master image of the pair

**Fig. 2.** Due to the seasonal difference between the pre- and post-event images, colored areas that were caused by the change in vegetation are observed in the suburbs of Kumamoto.

### 3. The Change Indices

The objective of this study is to grasp the damage situation soon after a disaster strikes. Thus, the simplest extraction method using threshold values of the change indices was adopted. Several change indices were proposed in previous studies [5–7]. Coherence and its extension factors, the coherence ratio and the normalized difference coherence index, are the reprehensive indices in the phase-base analysis. In the intensity-base analysis, the difference and the correlation coefficient are commonly used to evaluate the multitemporal changes. The  $z$ -factor, proposed by the present authors, is a combination of the difference and the correlation coefficient [17]. Owing to the sensitivity, the coherence obtained on an L-band SAR image makes it easier to assess the damage than it is on data acquired at C-band [18]. However, the previous L-band sensors (JERS-1, PALSAR) with their low resolution only enable damage assessment at the big block level. The utility of the  $z$ -factor in terms of extracting damage in a building unit from high-resolution TerraSAR-X images has been proven [19]. However, the validity of high-resolution L-band SAR images in damage extraction at the building level has not yet been reported. In this study, the coherence, the coherence ratio, and the  $z$ -factor were used to extract areas damaged in the Kumamoto earthquake.

#### 3.1. The Phase-Based Indices

The coherence ( $\gamma$ ) is the interferometric correlation between two SAR complex data, which is calculated by the ratio between coherent and incoherent summations, as in Eq. (1).

$$\gamma = \frac{\sum C_1 C_2}{\sqrt{\sum |C_1|^2} \sqrt{\sum |C_2|^2}}, \dots \dots \dots (1)$$

where  $C$  is a complex number with phase ( $\theta$ ) and magnitude ( $A$ ) [20].

The estimated absolute value of  $\gamma$ , which ranges between 0 and 1, is the function of systemic spatial decorrelation (noise) and temporal decorrelation between the master and slave acquisitions (geometrical decorrelation and temporal decorrelation). Due to the complicated decorrelation conditions, it is difficult to compare two coherences from different SAR pairs directly. Consequently, the coherence ratio was proposed to judge the coherence changes [18, 21].

To extract damaged areas from images after a disaster, the coherence can be obtained by one pre- and one post-event SAR data set. However, more than 3 images, commonly two pre-event images and one post-event image, are essential for the coherence ratio. In this study, the coherence was obtained in the slant range complex data. It was then projected with the pixel size of 2.5 m onto the base map. The coherence ratio was calculated from the geo-coded coherence data.

### 3.2. The Intensity-Based Indices

The difference ( $d$ ) and the correlation coefficient ( $r$ ) are calculated using Eqs. (2–3).

$$d = \bar{I}_b - \bar{I}_a, \dots \dots \dots (2)$$

$$r = \frac{N \sum_i I_a \cdot I_b - \sum_i I_a \sum_i I_b}{\sqrt{\left(N \sum_i I_a^2 - \left(\sum_i I_a\right)^2\right) \left(N \sum_i I_b^2 - \left(\sum_i I_b\right)^2\right)}} (3)$$

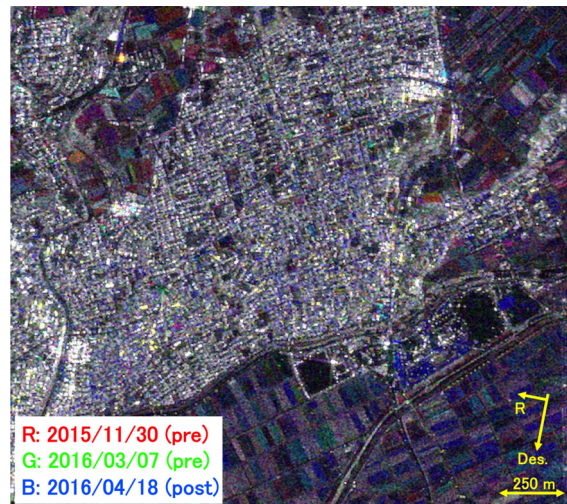
where  $i$  is the pixel number,  $I_{ai}$  and  $I_{bi}$  are the backscattering coefficients of the second (post) and first (pre) images, and  $I_a$  and  $I_b$  are the corresponding averaged values over the  $N = 5 \times 5$  pixel window surrounding the pixel  $i$ .

The difference and the correlation coefficient were calculated from the geo-coded intensity SAR images. Thus, the window size of  $12.5 \text{ m} \times 12.5 \text{ m}$  is close to the size of a residential lot. For a collapsed building, it is possible for there to be both the positive and negative changes in the SAR backscatter intensity. Thus, the large absolute difference value represents a high probability of changes. The correlation coefficient ranges between  $-1$  and  $1$ . The low value represents high possibility of changes. The absolute value of the difference and the correlation are combined into a new change index ( $z$ -factor) to describe the changes, as in Eq. (4) [16].

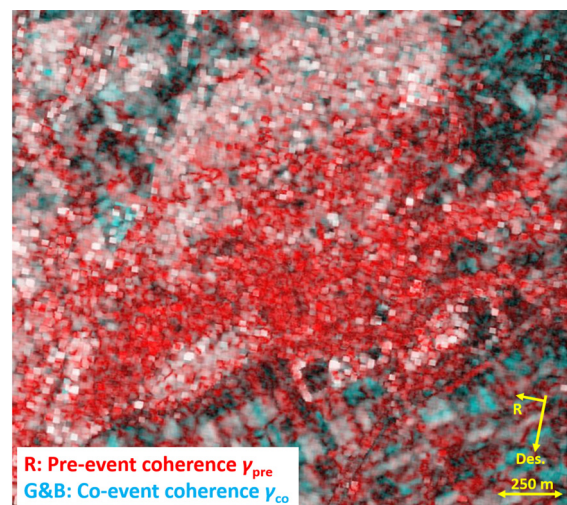
$$z = \frac{|d|}{\max(|d|)} - wr \dots \dots \dots (4)$$

where  $\max(|d|)$  is the maximum absolute value in difference and  $w$  is the weight between the difference and the correlation coefficient.

A weight of  $w = 0.5$  has been chosen in this study. Thus, the  $z$ -factor ranges between  $-0.5$  and  $1.5$ , where the high value represents a high probability of changes.



(a)



(b)

**Fig. 4.** Color composites of three temporal PALSAR-2 intensity images (a) in path 23, and the combination of the pre- and co-event geo-coded coherence (b) of the same pair data.

## 4. Experiments and Results

The adopted change indices, namely, the coherence ( $\gamma$ ), the coherence ratio and the  $z$ -factor, were calculated from the SAR pairs for the central part of Mashiki. The change indices obtained were compared with the reference data to investigate their relation to the damage levels. Then the target areas were classified into the different damage levels according to a suitable threshold value. The reference data were also used to examine the accuracy of the results. The change index with the best results for damage classification was applied to the whole DID study area.

### 4.1. The Pair Taken in Path 23

The color composite of the three PALSAR-2 images taken in the descending path 23 is shown in **Fig. 4(a)**. The two pre-event images were loaded in red and green, respectively, and the post-event image was loaded in blue. Due to the seasonal difference, a significant change in

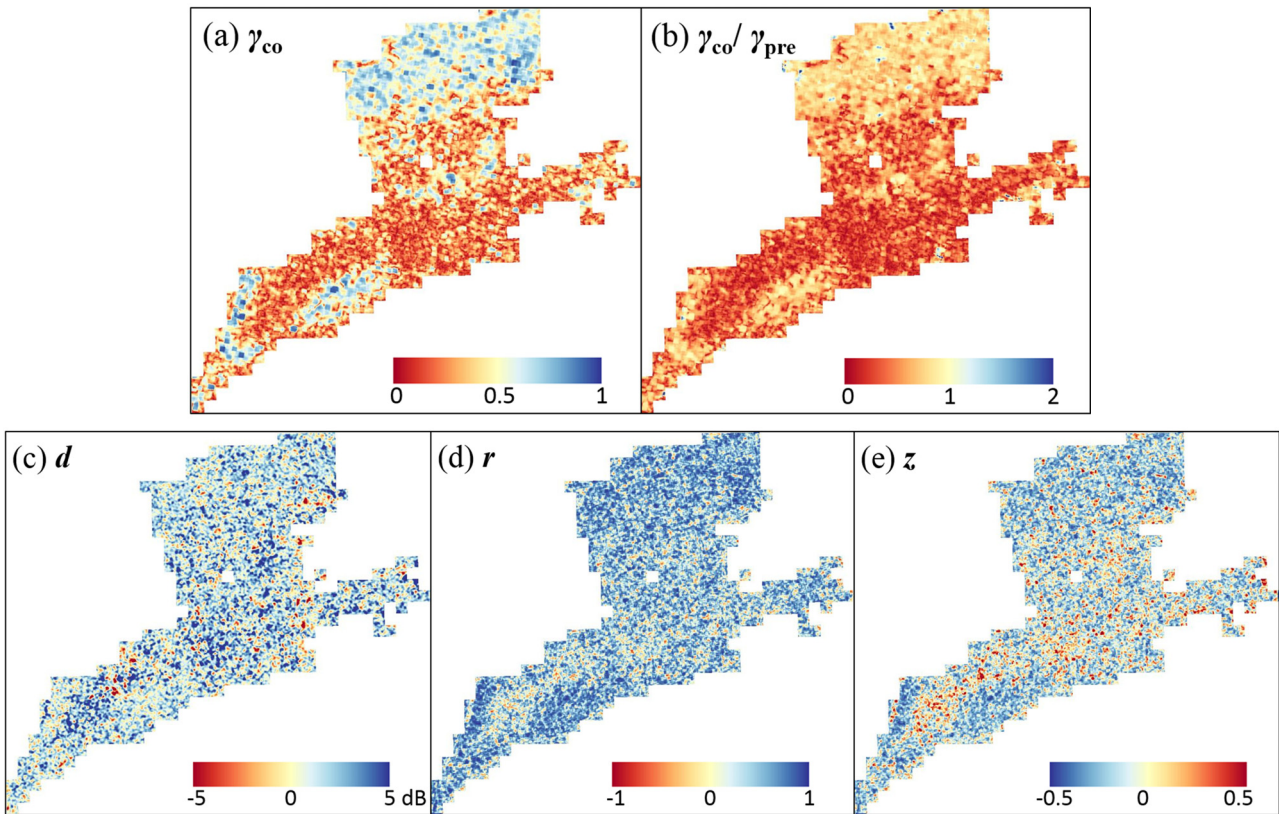


**Fig. 5.** Change indices calculated from the SAR pair in path 23, in the common region of the target area, and the reference data, shown in a red-blue map: (a) coherence, (b) coherence ratio, (c) difference, (d) correlation coefficient, and (e) z-factor.

the backscattering echo could be confirmed in agriculture fields. Several intensity changes were also shown in urban areas as yellow and blue regions, which were caused by damage to buildings.

The pre-event coherence ( $\gamma_{pre}$ ) between the image taken on March 7, 2016 (master) and the one on November 30, 2015 (slave) was calculated from the complex SAR data, and then it was geo-coded. The same approach was applied to the image taken on March 7, 2016 (master) and the one on April 18, 2016 (slave) to obtain the geo-coded co-event coherence ( $\gamma_{co}$ ). The color composite of the pre- and co-event coherences is shown in **Fig. 4(b)**. The urban areas commonly show high coherence values, close to 1, owing to stable backscatter from buildings. Significant decreases in the co-event coherence could be seen in a wide urban area shown in red.

The co-event coherence for the same urban area as the reference data is shown in **Fig. 5(a)** by a red and blue map. More than half of the target area is red, with the coherence close to 0. In addition, the locations of red-colored areas are similar to those of the high collapse-rate areas in **Fig. 3(c)**.

A coherence ratio between the co- and pre-event values ( $\gamma_{co}/\gamma_{pre}$ ) was also obtained, as seen in **Fig. 5(b)**. The ratio ranges between 0 and 780, but more than 99% of the area is less than 3. Values close to 1 indicate no change, values significantly less than 1 indicate a decrease, and values significantly larger than 1 indicate an increase in the coherence after the earthquake. In **Fig. 5(b)**, most of the

target area shows low values, less than 1.0. The low-value areas match the low co-event coherence areas.

The difference ( $d$ ) and the correlation coefficient ( $r$ ) were calculated from the images taken on March 7 and April 18, 2016, as shown in **Figs. 5(c)–(d)**. The difference was in the range from -19 dB to 17 dB. Since the smoothing window was relatively small ( $5 \times 5$  pixels), the changes in backscatter were obtained over most of the target area. The area of positive changes appears larger than that of negative changes. For the correlation coefficient, most of the area shows a higher correlation than 0. Compared with the reference data shown in **Fig. 3(c)**, the grid cells with high collapse ratios show low correlation, less than 0. Then the z-factor, which combines the difference and the correlation coefficient, was obtained, as shown in **Fig. 5(e)**. The red pixels with values larger than 0 were considered to have a high probability of change. This combined index more clearly highlights the changed areas and makes them more similar to the reference data.

#### 4.1.1. Examination of the Threshold Values

The profiles of the change indices, namely, the coherence, coherence ratio, and z-factor for each of the collapse levels from 0% to more than 75%, were investigated by comparing them with the reference data. The average values and the standard deviations are shown in **Fig. 6**. The coherence and the coherence ratio decrease as the collapse ratio increases, whereas the z-factor has an almost linear related.

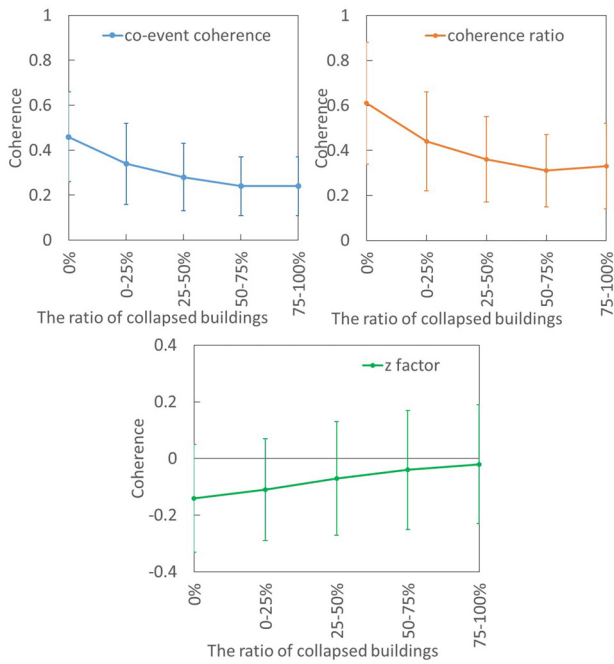


**Fig. 6.** Profiles of three change indices for the four different building collapse levels, which were obtained from the SAR pair taken in the path 23.

The average value of the coherence is 0.46 for the non-collapsed area, and it decreases to 0.24 for the “more than 50% collapsed” grid cells. The standard deviations for all the collapse levels are around 0.15. The average value of the coherence ratio is 0.61 for the “not collapsed” area, and it decreases to 0.31 for the “more than 50% collapsed” grid cells. The standard deviations are around 0.2. Compared with the profile of the coherence, the profile of the coherence ratio is more distinctive for the different collapse levels. The average value of the  $z$ -factor is  $-0.14$  for the “not collapsed” area, and it increases to  $-0.02$  for the “more than 75% collapsed” grid cells. The standard deviations for all the collapse levels are around 0.20. Compared with the differences in the average value for each collapse level, it is difficult to distinguish the different collapse levels from the  $z$ -factor, due to its large standard deviation. According to **Fig. 6**, the “50–75% collapsed” cells show similar profiles to the “more than 75% collapsed” cells, so they were merged into one damage level.

The probability function was introduced to examine the most suitable threshold values for the damage classification. For one change index value, the probabilities of the four collapse levels, 0%, 0–25%, 25–50%, and more than 50%, are calculated automatically according to the normal distribution using their average values and the standard deviations. When the probability density values for two neighboring collapse levels intersect, this boundary is defined as the threshold value, following the analogy with the maximum likelihood classification method. As a result, the threshold values of the coherence, the coherence ratio, and the  $z$ -factor for each building collapse level were obtained and are presented in **Table 2**.

**Table 2.** The threshold values of the change indices for the four different building collapse levels.

Change index	The building collapse level			
	0%	0-25%	25-50%	50-100%
Coherence	$> 0.40$	$> 0.30$	$> 0.26$	$> 0$
Coherence ratio	$> 0.52$	$> 0.40$	$> 0.34$	$> 0$
Z-factor	$< -0.12$	$< -0.08$	$< -0.05$	$< 1.50$

**Table 3.** The accuracy of the classification using the co-event coherence of the SAR pair in path 23, organized into four collapse levels.

Ratio of collapse	Reference data					UA
	0%	0-25%	25-50%	50-100%	Total	
0%	86572	9205	5635	3372	104784	82.6%
0-25%	19863	5337	5586	4793	35579	15.0%
25-50%	7160	2379	2950	3104	15593	18.9%
50-100%	26312	9574	14987	16829	67702	24.9%
Total	139907	26495	29158	28098	223658	
PA	61.9%	20.1%	10.1%	59.9%		49.9%

#### 4.1.2. Production of the Building-Collapse Map

The building collapse maps were then obtained using the defined threshold values. They were verified through comparison with the reference data. The accuracy of the result from the coherence value is shown in **Table 3**. The producer accuracy (PA) for the “not collapsed” areas and “more than 50% collapsed” areas are about 60%, whereas the accuracies for the “0–25% collapsed” and “25–50% collapsed” areas are lower than 21%. The user accuracy (UA) for the “not collapsed” cells was higher than 80%, whereas the accuracies for the building collapse areas are all less than 25%. Thus, using the coherence index, it is possible to distinguish the collapsed areas from those left intact, but it is difficult to classify the level of building damage in each grid cell. The overall accuracy is 49.9%.

Since the accuracy of the “25–50% collapsed” level is the lowest, there was an attempt to merge it with another damage level. The “25–50% collapsed” level was merged with the “0–25% collapsed” level and with the “more than 50% collapsed” level. Merging the “25–50% collapsed” level with the “more than 50% collapsed” level yields a higher accuracy, as shown in **Table 4(a)**. The accuracy for the most collapsed areas increased, but the UA is still less than 50%. The overall accuracy increases to 58.0%.

The overall accuracy of the classification using the coherence ratio is 52.3%. When the coherence ratio is used instead of co-event coherence, both the UA and the PA are higher for all the damage levels, except for the PA for the “0–25% collapsed” level. However, the accuracy for the damage level 25-50% was still the lowest, less than 20%, so this damage class was also merged with the “more than 50% collapsed” areas. The accuracy matrix is shown in **Table 4(b)**. In this result, the coherence is more useful for the damage classification, considering the acquisition possibility of SAR data.

The accuracy of the result using the  $z$ -factor is the low-

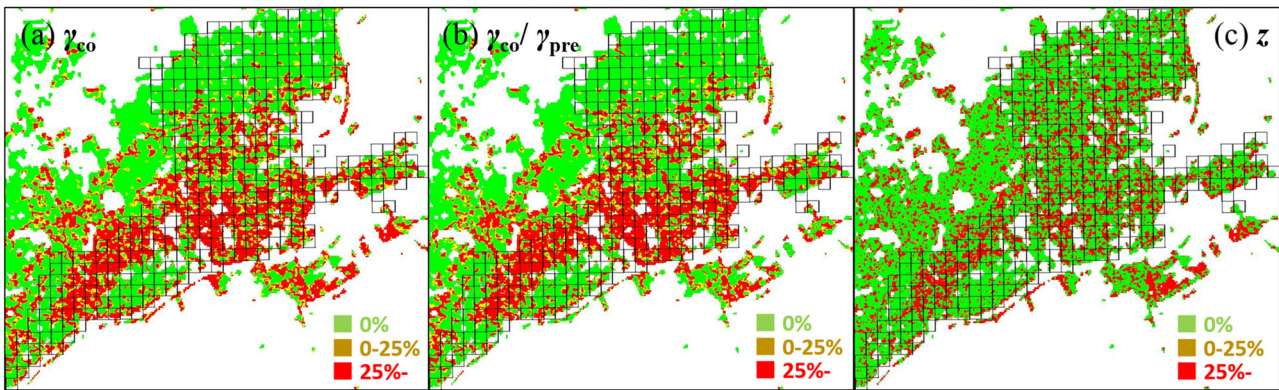


**Fig. 7.** The building collapse maps obtained in path 23 for the urban areas in Mashiki using (a) the coherence, (b) the coherence ratio, and (c) the z-factor values.

**Table 4.** The accuracy of the classifications using the (a) co-event coherence, (b) the coherence ratio, and (c) the z-factor into three collapse levels, from the SAR pair in path 23.

(a) coherence					
Ratio of collapse	Reference data			Total	UA
	0%	0-25%	25-100%		
0%	86572	9205	9007	104784	82.6%
0-25%	19863	5337	10379	35579	15.0%
25-100%	33472	11953	37870	33472	45.5%
Total	139907	26495	57256	223658	
PA	61.9%	20.1%	66.1%		<b>58.0%</b>

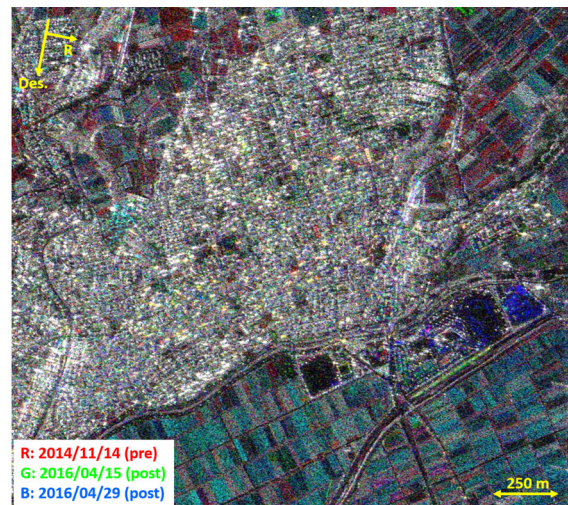
(b) coherence ratio					
Ratio of collapse	Reference data			Total	UA
	0%	0-25%	25-100%		
0%	91848	8984	9795	104784	83.0%
0-25%	17151	5051	9408	35579	16.0%
25-100%	30908	12460	38053	33472	46.7%
Total	139907	26495	57256	223658	
PA	65.6%	19.1%	66.5%		<b>60.3%</b>

(c) z-factor					
Ratio of collapse	Reference data			Total	UA
	0%	0-25%	25-100%		
0%	86382	14278	23576	104784	69.5%
0-25%	9552	1944	4373	35579	12.3%
25-100%	43973	10273	29307	33472	35.1%
Total	139907	26495	57256	223658	
PA	61.7%	7.3%	51.2%		<b>52.6%</b>

est even after the classes are merged, as shown in **Table 4(c)**. The overall accuracy is 52.6%. However, the PA for the “0-25% collapsed” level is less than 10%. Since the z-factor uses only the backscattering intensity, it is less sensitive than the coherence.

Since the reference map is the damaged building ratio (the number of collapsed buildings / the number of total buildings in a grid), whereas the coherence represents the damaged areas, the mismatch between the two data caused the lower accuracy. Additionally, the 57-m grid size was larger than the 12.5-m window size used for the PALSAR-2 images. There could be further discussion if there were a higher resolution reference, but the reference



**Fig. 8.** Color composites of the PALSAR-2 intensity images taken before (R), during (G) and after (B) the earthquake in path 28.

map is the only ground truth data that is currently available.

The building collapse map calculated from the three indices is shown in **Fig. 7**. An urban mask according to the land-cover map shown in **Fig. 3(b)** was introduced to remove the changes in vegetated areas. In the three results, only limited areas were classified into the “0–25% collapsed” level. The range of the reference data is shown as the black grid cells. The red areas with more than 25% building collapse in the results of the coherence and the coherence ratio show high agreement with the reference data. In contrast, the red areas obtained by the z-factor appear more scattered.

#### 4.2. The Pair Taken in Path 28

The color composite of the three PALSAR-2 images taken in the descending path 28 is shown in **Fig. 8**. The images taken before, during, and after the earthquake are loaded in red, green, and blue, respectively. Several yellow and blue regions, which are considered as changed after the mainshock, can be confirmed in the urban areas.

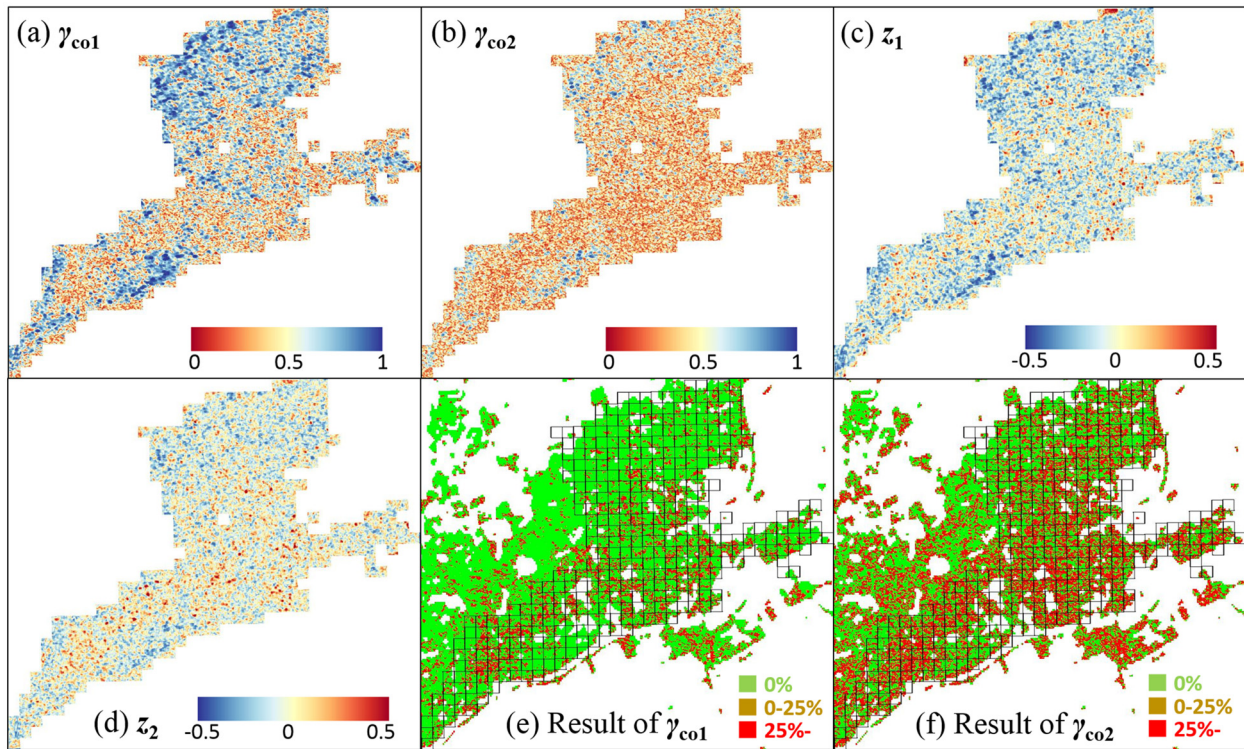


**Fig. 9.** Change indices calculated from the SAR pair in Path 28 shown in a red-blue color table: (a) the first co-event coherence; (b) the second co-event coherence; (c) the first  $z$ -factor; (d) the second  $z$ -factor. The building collapse maps obtained for the urban areas in Mashiki using the first and the second co-event coherence (e-f).

The first co-event coherence ( $\gamma_{co1}$ ) between the image on November 14, 2014 (master) and the one on April 15, 2016 (slave) was calculated and geo-coded. The second co-event coherence ( $\gamma_{co2}$ ) between the same master image and the image on April 29, 2016 (slave) was also obtained. The two co-event coherences in the same area of the reference data are shown in **Figs. 9(a)–(b)**. More than half of the target areas show low coherence, around 0, in both pairs. As the pre-event image was taken one year before the other images, the decorrelation was caused by both the long time lag and the damage. The effect of the long time-lag occupies the de-correlation in **Fig. 9(b)**.

The profiles of the coherence from the second co-event pair were investigated by introducing the reference data. The average value for the “not collapsed” grid cells is 0.43, whereas it decreases to 0.36 for the “more than 25% building collapse” cells. The standard deviation is around 0.17. Compared with the profile of the pairs taken in path 23, the collapse levels of the pair taken in path 28 are more difficult to separate. The threshold value for separating the “not collapsed” level from the “collapse level” was defined as 0.42. When the coherence was less than 0.38, the pixel was put into the “more than 25% building collapsed” class.

The building collapse map that was obtained is shown in **Fig. 9(f)**. Most of the common area with the reference data was classified as “more than 25% building collapsed,” which is an overestimation. The confusion matrix obtained is shown in **Table 5**. The accuracies of all the “collapse” classes are lower than they are in the results of the co-event coherence taken in path 23. The overall

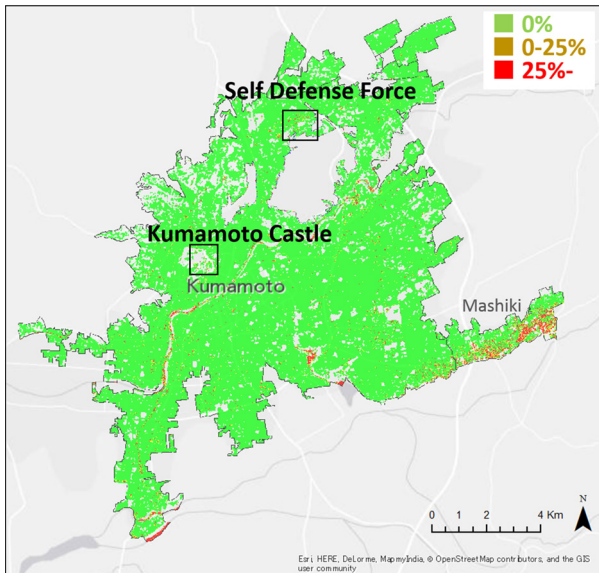
**Table 5.** The accuracy of the damage classifications using the co-event coherence obtained from the SAR pair in path 28.

Ratio of collapse	Reference data			Total	UA
	0%	0-25%	25-100%		
0%	70491	11780	20321	102592	68.7%
0-25%	10367	2142	4824	17333	12.4%
25-100%	59049	12573	32111	103733	31.0%
Total	139907	26495	57256	223658	
PA	50.4%	8.1%	56.1%		<b>46.8%</b>

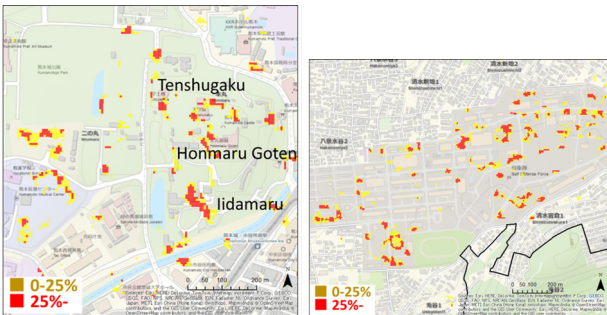
accuracy is 46.8%, less than 50%.

The same threshold values were applied to the first co-event pair to detect the damage situation after the foreshock, as shown in **Fig. 9(e)**. Since there were no truth data for the damages after the foreshock, truth data accuracy could not be verified. As there is only one pre-event image in path 28, it is impossible to calculate the coherence ratio.

The  $z$ -factor for the two co-event pairs was also obtained in **Figs. 9(c)–(d)**. As in the case of coherence, the color of most of the target area indicates change after the mainshock. Both results are more overestimated than the reference data. The profiles of the three collapse levels were output. The increase of the  $z$ -factor from the “not collapsed” level to the “more than 25% collapsed” level is only 0.02, too small for the 0.16 standard deviation. Thus, it is difficult to classify the collapse level using these  $z$ -factor values.



(a)



(b) Kumamoto Castle

(c) Self Defense Force

**Fig. 10.** (a) Building collapse map for urban areas in all affected DID areas in Kumamoto Prefecture using the co-event coherence of the SAR pair in the path 23, (b) enlarged area for Kumamoto Castle, and (c) enlarged area for the Self Defense Force.

### 4.3. The Application of DID

The coherence ratio of the SAR pair taken in path 23 obtained the best result of the classifications in the previous section. However, the coherence of the co-event pair in path 23 also yielded suitable results even though only two images were used. According to the previous study [22], a combination of the indices calculated from different paths would increase the accuracy of the building damage extraction. The combination of the co-event coherence in paths 23 and 28 was attempted. However, affected by the decorrelation of the pair in path 28, the accuracy of the combination was lower than when only the co-event coherence of path 23 was used.

Thus, the co-event coherence of path 23 was applied to the entire study area. The resultant building collapse map of Kumamoto and surrounding areas is shown in Fig. 10(a). The land-cover map was introduced to remove the effects of vegetation change. Fig. 10(a) shows that the areas of building collapse were concentrated in Mashiki. Most of Kumamoto was not affected. Several river regions are in red due to the changes in water level

and the mismatch of the land-cover map and the SAR images. These results show high agreement with the field survey [23].

Two enlarged regions with dense collapse areas are shown in Figs. 10(b)–(c). These areas are Kumamoto Castle and the North Kumamoto base of the Japan Ground Self Defense Force. For Kumamoto Castle, the damage to the Main Tower and Goten (palace building) in the Honmaru (main) area as well as the damage in the Idamaru area were detected successfully. The changes of cars in the parking lots in the Ninomaru area and in the Kumamoto Medical Center are also classified as damages. In the Self Defense Force base, many collapsed areas are mistakenly extracted. These changes are caused by vehicles and tents associated with the earthquake response activities. If only the coherence information is used, these changes cannot be separated from building damage. However, the introduction of building footprint data promises to improve future damage probability maps.

## 5. Conclusion

In this study, the areas with collapsed buildings in the affected DID areas in Kumamoto Prefecture were extracted from six pre- and post-event ALOS-2 PALSAR-2 images. Three representative change indices, namely, the coherence, the coherence ratio, and the z-factor (combination of the difference and the correlation coefficient), were adopted to evaluate the building collapse level of city blocks. The profiles of the change indices for each damage level were investigated by introducing reference data from field surveys. Then, the threshold values for classifying the different collapse levels were estimated. The building collapse maps for Mashiki Town were produced and verified using the reference data. Finally, the co-event coherence of the SAR pair in path 23 was selected as the most effective index, as it yielded an overall accuracy of 58%. It was then applied to the entire DID area under study.

Although the co-event coherence classified the region into intact and collapsed areas highly accurately, its efficiency was affected by the acquisition condition. If the decorrelation of the coherence is contaminated by other elements, e.g., time lag or noise, its accuracy declines. The low coherence can be used to detect areas of change, but it is still difficult to distinguish building damage from normal changes. In the future, the proposed building collapse map can be improved by imposing building footprints. Its accuracy may be verified by comparing it with other truth data, e.g., aerial photographs or airborne Lidar data.

### Acknowledgements

The ALOS-2 PALSAR-2 data used in this study are owned by the Japan Aerospace Exploration Agency (JAXA) and were provided through JAXA's 4th ALOS-2 Research Announcement (RA-4), PI Number 1503 (F. Yamazaki). This study was financially supported by a Grant-in-Aid for Scientific Research (Project num-

bers: 15K16305 and 24241059) and the Core Research for Evolutional Science and Technology (CREST) program by the Japan Science and Technology Agency (JST) "Establishing the most advanced disaster reduction management system by fusion of real-time disaster simulation and big data assimilation (Research Director: Prof. Shunichi Koshimura of Tohoku University)."

#### References:

- [1] United States Geological Survey (USGS): <https://earthquake.usgs.gov/earthquakes/eventpage/us20005iis#executive> [accessed]
- [2] Cabinet Office of Japan (2016) Summary of damage situation in the Kumamoto earthquake sequence: <http://www.bousai.go.jp/updates/h280414jishin/index.html> [accessed]
- [3] QuiQuake: <https://gbank.gsj.jp/QuiQuake/index.en.html> [accessed]
- [4] Japan Meteorological Agency (JMA): [http://www.jma.go.jp/jma/en/2016\\_Kumamoto\\_Earthquake/2016\\_Kumamoto\\_Earthquake.html](http://www.jma.go.jp/jma/en/2016_Kumamoto_Earthquake/2016_Kumamoto_Earthquake.html) [in Japanese, accessed]
- [5] L. Dong and J. Shan, "A comprehensive review of earthquake-induced building damage detection with remote sensing techniques," *ISPRS J. Photogramm. Remote Sens.*, Vol.84, pp. 85-99, 2013.
- [6] P.T.B. Brett and R. Guida, "Earthquake damage detection in urban areas using curvilinear features," *IEEE Trans. Geosci. Remote Sens.*, Vol.51, pp. 4877-4884, 2013.
- [7] S. Plank, "Rapid damage assessment by means of multi-temporal SAR: A comprehensive review and outlook to Sentinel-1," *Remote Sens.*, Vol.6, pp. 4870-4906, 2014.
- [8] ALOS Research and Application Project of EORC, JAXA: [http://www.eorc.jaxa.jp/ALOS/lulc/jlulc\\_jpn.htm](http://www.eorc.jaxa.jp/ALOS/lulc/jlulc_jpn.htm) [accessed]
- [9] M. Matsuoka and M. Estrada, "Development of earthquake-induced building damage estimation model based on ALOS/PALSAR observing the 2007 Peru earthquake," *J. of Disaster Research*, Vol.8, No.2, pp. 346-355, 2013.
- [10] S. Park, Y. Yamaguchi and D. Kim, "Polarimetric SAR remote sensing of the 2011 Tohoku earthquake using ALOS/PALSAR," *Remote Sensing of Environment*, Vol.132, pp. 212-220, 2013.
- [11] M. Watanabe, T. Motohka, Y. Miyagi, C. Yonezawa and M. Shimada, "Analysis of urban areas affected by the 2011 off the Pacific coast of Tohoku earthquake and tsunami with L-Band SAR full-polarimetric mode," *IEEE Geosci. and Remote Sens. Letters*, Vol.9, No.3, pp. 472-476, 2012.
- [12] R. Bahri, W. Liu and F. Yamzaki, "Damage assessment of urban areas due to the 2015 Nepal earthquake using PALSAR-2 imagery," in *Proc. 36th Asia Conf. on Remote Sensing (ACRS)*, 2015.
- [13] M. Watanabe, R.B. Thapa, T. Ohsumi, H. Fujiwara, C. Yonezawa, N. Tomii and S. Suzuki, "Detection of damaged urban areas using interferometric SAR coherence change with PALSAR-2," *Earth, Planets and Space*, Vol.68, No.131, 2016.
- [14] S. Hashimoto, T. Tadono, M. Onosato, M. Hori and K. Shiomi, "A new method to derive precise land-use and land-cover maps using multi-temporal optical data," *J. of The Remote Sensing Society of Japan*, Vol.34, No.2, pp. 102-112, 2014 (in Japanese).
- [15] Geospatial Information Authority of Japan (GSI): <http://fgd.gsi.go.jp/download/menu.php> [accessed]
- [16] National Institute for Land and Infrastructure Management (NILIM), "Quick report of the field survey on the building damage by the 2016 Kumamoto earthquake," technical Note No.929, <http://www.nilim.go.jp/lab/bcg/siryou/tnn/tnn0929.htm> [in Japanese, accessed]
- [17] W. Liu and F. Yamazaki, "Urban monitoring and change detection of central Tokyo using high-resolution X-band SAR images," in *Proc. IEEE Int. Geoscience and Remote Sensing Symposium*, pp. 24-29, 2011.
- [18] Y. Ito, M. Hosokawa, H. Lee and J.G. Liu, "Extraction of damaged regions using SAR data and neural networks," *Int. Arch. Photogramm. Remote Sens.*, XXXIII, pp.156-163, 2000.
- [19] W. Liu, F. Yamazaki, H. Gokon and S. Koshimura, "Extraction of Tsunami-Flooded Areas and Damaged Buildings in the 2011 Tohoku-Oki Earthquake from TerraSAR-X Intensity Images," *Earthquake Spectra*, EERI, Vol.29, No.S1, S183-S200, 2013.
- [20] A. Ferretti, A. Monti-Guarnieri, C. Prati, F. Rocca, Part C InSAR processing: a mathematical approach, In *InSAR Principles: Guidelines for SAR Interferometry Procs. and Interpretation*, K. Fletcher, Ed., ESA Publications: Noordwijk, Netherlands, pp. 3-13, 2007.
- [21] Y. Ito and M. Hosokawa, "Damage Estimation Model Using Temporal Coherence Ratio," in *Proc. IEEE IGARSS*, pp. 2859-2861, 2002.
- [22] H. Miura, S. Midorikawa, and M. Matsuoka, "Accuracy improvement of building damage detection using high-resolution SAR images observed from different directions," *J. of Japan Association for Earthquake Engineering*, Vol.15, No.7, pp. 7.390-7.403, 2015. (in Japanese)

- [23] F. Yamazaki and W. Liu, "Remote sensing technologies for post-earthquake damage assessment: A case study on the 2016 Kumamoto earthquake," in *Proc. 6th Asia Conf. on Earthquake Engineering (6ACEE)*, 2016.



**Name:**  
Wen Liu

**Affiliation:**  
Assistant Professor, Graduate School of Engineering, Chiba University

**Address:**  
1-33 Yayoi-cho, Inage-ku, Chiba 263-8522, Japan

**Brief Career:**  
2010-2013 Ph. D. of Engineering, Chiba University  
2013-2014 JSPS Postdoctoral Fellowship for Foreign Researchers, Tokyo Institute of Technology  
2014- Assistant Professor, Graduate School of Engineering, Chiba University

**Selected Publications:**

- "Estimation of three-dimensional crustal movements in the 2011 Tohoku-oki, Japan earthquake from TerraSAR-X intensity images," *Natural Hazards and Earth System Sciences*, Vol.15, pp. 637-645, 2015.
- "Extraction of Tsunami Flooded Areas and Damaged Buildings in the 2011 Tohoku, Japan Earthquake from TerraSAR-X Intensity Images," *Earthquake Spectra*, EERI, Vol.29, No.S1, pp. S183-2000, 2013.

**Academic Societies & Scientific Organizations:**

- Japan Society of Civil Engineers (JSCE)
- Remote Sensing Society of Japan (RSSJ)
- Institute of Electrical and Electronics Engineers (IEEE)



**Name:**  
Fumio Yamazaki

**Affiliation:**  
Professor, Department of Urban Environment Systems, Chiba University

**Address:**  
1-33 Yayoi-cho, Inage-ku, Chiba 263-8522, Japan

**Brief Career:**  
1978- Research Engineer, Shimizu Corporation, Japan  
1989- Associate Professor, Institute of Industrial Science, University of Tokyo  
2001- Professor, Asian Institute of Technology (AIT), Bangkok, Thailand  
2003- Professor, Department of Urban Environment Systems, Chiba University

**Selected Publications:**

- W. Liu and F. Yamazaki, "Detection of Crustal Movement from TerraSAR-X intensity images for the 2011 Tohoku, Japan Earthquake," *Geoscience and Remote Sensing Letters*, Vol.10, No.1, pp. 199-203, 2013.
- A. Meslem, F. Yamazaki, and Y. Maruyama, "Accurate evaluation of building damage in the 2003 Boumerdes, Algeria earthquake from QuickBird satellite images," *J. of Earthquake and Tsunami*, Vol.5, No.1, pp. 1-18, 2011.

**Academic Societies & Scientific Organizations:**

- Japan Society of Civil Engineers (JSCE)
- American Society of Civil Engineering (ASCE)
- Seismological Society of America (SSA)
- Earthquake Engineering Research Institute, USA (EERI)